Surface-resolved dynamic simulation of charged non-spherical particles

Xuan Ruan [a,b], Matthew T. Gorman [b], Shuiqing Li [a], Rui Ni [b,*]

[a] *Key Laboratory for Thermal Science and Power Engineering of Ministry of Education, Department of Energy and Power Engineering, Tsinghua University, Beijing 100084, China*
[b] *Department of Mechanical Engineering, Johns Hopkins University, Baltimore, MD 21218, USA*

ARTICLE INFO

ABSTRACT

We present a numerical method for simulating the electrostatic interaction of a cluster of charged non-spherical particles as they collide with each other. The boundary element method (BEM) is employed to resolve the highly nonuniform surface charge distribution on individual particles, based on which their electrostatic interactions can be computed. The method of generalized minimum residual (GMRES) incorporated with the fast multipole method (FMM) is adopted to accelerate the electrostatic calculation. The framework is validated through four different cases and is proven to capture the induced higher-order multipole interaction as two particles become very close to each other. This interaction is also shown to be sensitive to the particle geometry, in particular the local curvatures. In addition to the electrostatic interactions, the contact forces and torques are included using the Hertzian contact model to capture the particle collision. Finally, this comprehensive framework is demonstrated by reproducing typical collision outcomes, e.g., sticking and fragmentation, among several non-spherical charged particles.

© 2022 Elsevier Inc. All rights reserved.

1. Introduction

The electrostatic interaction among particles in multiphase flow systems is ubiquitous in natural and industrial applications, from planet formation [28,49], sediment transport [19], ash aggregation in volcanic plumes [50] to engineering systems, such as suspensions of charged colloidal particles [2], particulate matters control [22,10], and powder build-up in conveying tubes [48]. In many cases, the electrostatic interactions become comparable to or even stronger than other forces, which leads to significant changes in particle behaviors. For instance, the binding energy of charged grains has been reported to be three orders of magnitude larger than the short-range cohesion in granular streams [28]. In particle-laden flows, the Coulomb repulsion repels like-charged particles and delays the pore clogging [10], whereas the dipolar interaction could effectively attract incoming particles and promote pore clogging [43]. The dielectric effects have also been found to significantly alter the self-assembly of colloidal aggregates [3]. Furthermore, particles participating in almost all these processes have non-spherical geometries, and their surface roughness can be so large that it severely modulates particle-particle interactions.

In systems containing a large number of particles, dielectric particles are often treated as point charges for simplicity, and their interaction can be simplified as a pairwise Coulomb interaction [35,13,49,46]. When particles are close to each other,

* Corresponding author.
    E-mail address: rui.ni@jhu.edu (R. Ni).

in addition to the Coulomb interaction, particles will induce charges on each other, and the problem becomes much more complicated. In particular, in the presence of an external field, there is a relative shift of the positive and negative charges to the opposing ends of the particles. One approximation that has often been used in various simulations to capture such a shift is the induced dipole model, which simplifies a polarized particle by a dipole. By using the induced dipole model, abundant phenomena have been reported in both dilute and dense particle-laden flows [34,26] revealing the essential influence of particle polarization.

Nevertheless, the induced dipole moment is only the first-order approximation of the non-uniform charge distribution on the particle surface, which limits its accuracy when induced higher-order multipoles are important [3,28]. Hence, for decades researchers have been devoted to finding more precise description of the electrostatic interactions. For simple geometries, such as a pair of spheres or a sphere near a surface, analytic solutions have been proposed to calculate the electrostatic interactions. Typical examples include the image charge method [31,40,41] and the re-expansion method [53, 39,7]. Although the analytic solutions provided accurate predictions of the electrostatic interactions in simple systems and reveal the importance of the induced higher-order multipoles to some extent, it is generally difficult to directly apply these solutions to multiple-particle systems [44] or to non-spherical geometries.

To address this issue, different numerical methods have been developed and are becoming more promising with the growth of the computing power. To compute the electrostatic interaction between a collection of spheres, Lindgren et al. [32] presented the Galerkin approximation based on the truncated spherical harmonics series. This approximation method was further employed in the dynamic simulations of the self-assembly and aggregation of charged dielectric spheres [33]. This method was proven to be accurate and efficient, but limited only to spherical particles.

In addition, the finite element method (FEM) is also employed to compute the electrostatic interactions. The domain, including both particles and the space in between, is generally discretized into a regular grid on which the electrostatic problem is solved. The electrostatic interaction on each particle can then be obtained by integrating over the surface elements. Compared to the analytic solutions, FEM can be applied to more complicated geometries and multi-particle interactions. Feng [14] first used FEM to calculate the electrostatic force between two touching dielectric spheres in a 2D domain. Recently, this method has been further extended to study the electrostatic attraction among up to tens of charged particles in a 3D domain [37].

If the geometry boundaries are sharp, the charge density reduces to the surface charge density, which significantly simplifies the electrostatic problem. Instead of discretizing the 3D domain, we only need to dicretize the particle surfaces and calculate the surface charge distribution. The electrical field at a certain point can then be obtained by summing the contribution over all the surface elements. This boundary element method (BEM) is of high efficiency and has been employed to simulate the self-assembly in colloids [4,3].

So far, the BEM simulations focus primarily on the electrostatic interaction of charged dielectric spheres, and the more general non-spherical particles have not been considered. Besides, for solid particles suspended in the gaseous flows or in the vacuum, the contact force between colliding particles should play a crucial part in aggregation and triboelectrification [17,25]. Therefore, a numerical model integrating both the electrostatic interaction and the contact force is desired to understand the underlying physics. In this study, we present a framework to conduct dynamic simulation of charged dielectric ellipsoidal particles. The boundary element method is adopted on a triangular mesh to solve the particle surface charge distribution, the integration of which results in the electrostatic interaction. In addition, to solve the collision process, the ellipsoids are treated as soft particles and the contact interactions are resolved based on the Hertzian theory. Special attention is paid to non-dimensionalizing particle's momentum equation to ensure that the electrostatic interaction is scaled appropriately when the particle stiffness is adjusted to accelerate calculations. Different validation cases are shown to support the validity of the framework and how the particle geometry impacts the electrostatic interaction. Furthermore, the dynamic simulations of the particle-aggregate collision are performed with different post-collision outcomes, e.g., sticking and fragmentation, to show the effect of the electrostatic interaction and contact force in the aggregation process.

2. Methods

2.1. Electrostatic interactions between ellipsoids

2.1.1. Boundary element method

A dielectric particle can be polarized by an external electric field. This polarization and the associated induced bound charges of an individual particle produces a separate electric field. For two dielectric particles interacting with each other, the calculation becomes coupled, and the traditional method that involves Coulomb and dipole interactions may require iteration to find the solution [26]. In this study, we employ the framework proposed by Barros et al. [4], Barros and Luijten [3] to efficiently resolve the multipole electrostatic interactions between dielectric particles without any iteration. Here, we briefly derive the governing equation, and detailed information can be found in the references above.

The electric field $\mathbf{E}$ is associated with the volumetric charge density ρ as

$$\nabla \cdot \mathbf{E} = \rho/\varepsilon_0 = (\rho_f + \rho_b)/\varepsilon_0, \tag{1}$$

where ε_0 is the vacuum permittivity, ρ_f and ρ_b are the free and bound charge volumetric density, respectively. For an idealized medium, the polarization $\mathbf{P}$ is proportional to the external field
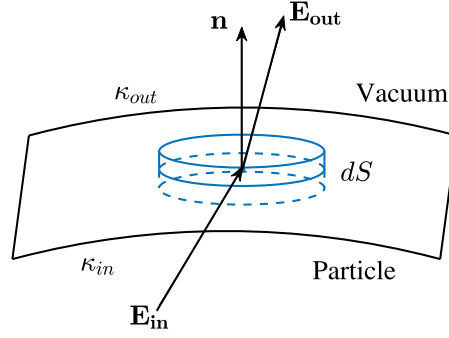
Fig. 1. Schematic of the control volume on the particle surface. The outward unit vector points from the particle to the medium.

$$\mathbf{P} = \varepsilon_0(\kappa - 1)\mathbf{E}. \tag{2}$$

where κ is the dielectric constant of the medium. The polarization is also related to the bound charge volumetric density ρ_b following

$$\nabla \cdot \mathbf{P} = -\rho_b. \tag{3}$$

Combining Eqs. (1), (2) and (3) then yields

$$\rho_f = \varepsilon_0 \nabla \cdot (\kappa \mathbf{E}). \tag{4}$$

In this study, we focus on the electrostatic interactions between dielectric particles in vacuum. Since the dielectric constant only changes at the particle-vacuum interface, the charge volumetric density ρ simplifies to the charge surface density σ. To derive the governing equation of σ, we choose a flat cylindrical control volume on the particle-vacuum interface, as shown in Fig. 1. Integrating Eq. (4) over the control volume

$$\int_V \rho_f dV = \int_V \varepsilon_0 \nabla \cdot (\kappa \mathbf{E}) dV = \varepsilon_0 \int_S \kappa \mathbf{E} \cdot \mathbf{n} dS$$

yields

$$\sigma_f(\mathbf{r}) = \varepsilon_0(\kappa_{out}\mathbf{E}_{out} - \kappa_{in}\mathbf{E}_{in}) \cdot \mathbf{n}. \tag{5}$$

Here, $\mathbf{n}$ is the outward normal vector on the particle surface. By applying a similar process to Eq. (1), we obtain

$$\sigma_f(\mathbf{r}) + \sigma_b(\mathbf{r}) = \varepsilon_0(\mathbf{E}_{out} - \mathbf{E}_{in}) \cdot \mathbf{n}, \tag{6}$$

where $\sigma_f(\mathbf{r})$ and $\sigma_b(\mathbf{r})$ are the free and bound surface charge density. Taking Eq. (5) into Eq. (6) gives

$$\overline{\kappa}(\sigma_f + \sigma_b) + \varepsilon_0\Delta\kappa\mathbf{E} \cdot \mathbf{n} = \sigma_f, \tag{7}$$

where $\mathbf{E} = (\mathbf{E}_{out} + \mathbf{E}_{in})/2$ is the local field strength. $\overline{\kappa} = (\kappa_p + \kappa_0)/2$ and $\Delta\kappa = \kappa_0 - \kappa_p$ are the average and difference of the dielectric constants, respectively. After rearranging Eq. (7), the governing equation of the bound charge is given by

$$\mathcal{A}\sigma_b = b, \tag{8}$$

where the left side can be expanded into

$$\mathcal{A}\sigma_b = \overline{\kappa}\sigma_b + \varepsilon_0\Delta\kappa\mathbf{E}_b \cdot \mathbf{n}, \tag{9}$$

and the right side follows $b = (1 - \overline{\kappa})\sigma_f - \varepsilon_0\Delta\kappa\mathbf{E}_f \cdot \mathbf{n}$. Here, $\mathbf{E}_b(\mathbf{r}_i)$ is the electric field at $\mathbf{r}_i$ induced by all other bound charges at $\mathbf{r}_j$, which reads

$$\mathbf{E}_b(\mathbf{r}_i) = \int_S \frac{\mathbf{r}_i - \mathbf{r}_j}{4\pi\varepsilon_0|\mathbf{r}_i - \mathbf{r}_j|^3}\sigma_b(\mathbf{r}_j)dS. \tag{10}$$

$\mathbf{E}_f$ is the electric field induced by the free charge density σ_f that can be obtained similar to Eq. (10). In the simulation, the free charge σ_f is assumed to be uniformly distributed on the surface, and Eq. (8) is solved to obtain the bound charge density σ_b. This assumption is the first-order approximation of the surface charge distribution, which was shown to work well in estimating the net charge. For instance, such an assumption was employed in the study of the aggregation of
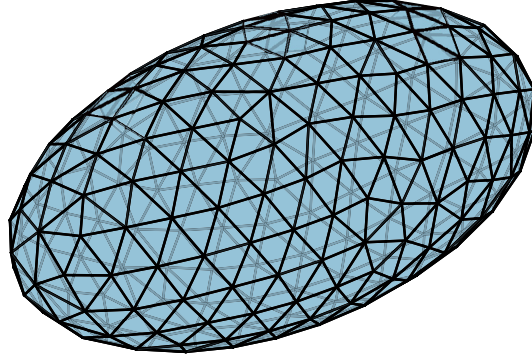
Fig. 2. Schematic of the triangular surface patches.

charged grains [28]. The predicted trajectories of grain pairs and the assembly of multiple particles agreed well with the experimental observations. However, it should be noted that the free charge distribution in many other scenarios, e.g. contact electrification, is often random [5], and a different free charge distribution should be selected. Since the free charge distribution is a user-defined quantity, which distribution one chooses does not affect the numerical framework introduced here.

Eq. (8) effectively separates the unknowns σ_b and $\mathbf{E}_b$ from the knowns σ_f and $\mathbf{E}_f$, and the entire equation can be used to solve the surface charge density over many discretized patches distributed on either one particle or multiple particles. In particular, for solving the electrostatic interaction among multiple charged particles in a cluster or in close proximity with each other, the equation still holds and the only change is to add surface patches of all particles into Eq. (8). Ultimately, it does not matter for the equation which particle one surface patch belongs to. They all interact with one another following the same rule. As a result, instead of iteratively solving particle-particle interactions, we solve a large matrix of $\mathcal{A}$.

Once σ_b is known, the electrostatic force $\mathbf{F}_E$ and torque $\mathbf{M}_E$ can be computed by integrating the force and torque over the surface of each particle following

$$\mathbf{F}_E = \int_S \kappa_0(\sigma_f + \sigma_b)\mathbf{E}dS, \tag{11a}$$

$$\mathbf{M}_E = \int_S \kappa_0(\sigma_f + \sigma_b)\mathbf{r} \times \mathbf{E}dS. \tag{11b}$$

2.1.2. Surface discretization

For non-spherical geometries, Eq. (8) must be solved along the surface to resolve the charge distribution. Here, we consider the simplest non-spherical shape, the ellipsoid. In Fig. 2, an ellipsoidal surface is discretized into triangular surface patches using the open-source code *DistMesh* developed by Persson and Strang [42]. For this method, the vertices adjust their positions dynamically under the repulsive force exerted by other adjacent vertices. The equilibrium is reached as the vertices become nearly equidistant and the area of each patch is almost the same. Then the matrix in Eq. (8) can be discretized as $\mathcal{A}_{ij} = \overline{\kappa}_i\delta_{ij} + \Delta\kappa_i\mathbf{n}_i \cdot \mathcal{I}_{ij}a_j$, where a_j is the surface area of the jth patch and $\mathcal{I}_{ij}$ is the Green function from the jth patch to the ith patch:

$$\mathcal{I}_{ij} = (\mathbf{r}_i - \mathbf{r}_j)/4\pi\left|\mathbf{r}_i - \mathbf{r}_j\right|^3 \tag{12}$$

The Green function becomes singular when considering the contribution of each patch to itself ($\mathcal{I}_{ii}$). In the present study, this self contribution is omitted by setting $\mathcal{I}_{ii} = \mathbf{0}$.

2.1.3. GMRES-FMM coupled calculation

As suggested by Barros et al. [4], instead of directly calculating the inverse matrix A^{-1}, the method of generalized minimum residual (GMRES) is used to solve the discrete form of Eq. (8). In the mth GMRES iteration, the mth-order Krylov subspace is generated as

$$K_m = span\{\mathbf{b}, \mathcal{A}\mathbf{b}, ..., \mathcal{A}^{m-1}\mathbf{b}\}. \tag{13}$$

Then the approximated solution $\sigma_b^{(m)}$ is obtained in K_m by solving the least square problem

$$min\|\mathbf{r}^{(m)}\| = min\|\mathbf{b} - \mathcal{A}\sigma_b^{(m)}\|. \tag{14}$$
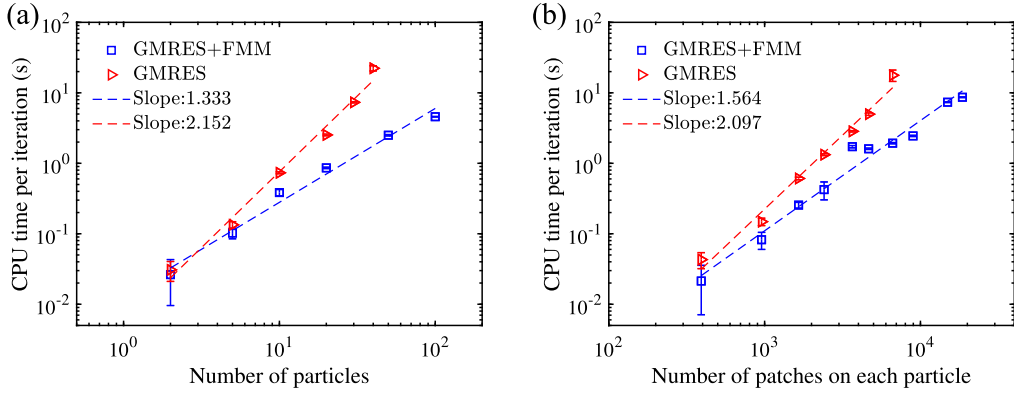
Fig. 3. Dependence of CPU time of every GMRES iteration on (a) the number of particles and (b) the number of surface patches.

Since $K_m \supset K_{m-1}$, the residual will decrease monotonically as $\|\mathbf{r}^{(m)}\| \leq \|\mathbf{r}^{(m-1)}\|$. When the relative tolerance is smaller than the preset criterion $\|\mathbf{r}^{(m)}\|/\|\mathbf{b}\| < 10^{-4}$, the solution converges.

The most expensive section in the mth iteration is to calculate the matrix-vector product $\mathcal{A}^{m-1}\mathbf{b} = \mathcal{A} \times \mathcal{A}^{m-2}\mathbf{b}$ in Eq. (13). Since each patch interacts with every other patch, the calculation cost of the matrix-vector product scales as $O(N^2)$ with N being the total number of surface patches in the system or the dimension of $\mathcal{A}$. As the particle number becomes larger or a finer mesh is employed, the calculation becomes increasingly more expensive. We decide to accelerate this procedure by implementing the fast multipole method (FMM) [16] because the operation of $\mathcal{A}^{m-1}\mathbf{b}$ is a forward problem similar to the electrostatic equation in Eq. (9).

The present code is written in MATLAB and run on a typical desktop with Intel(R) Core(TM) i7-8700 CPU at 3.20 GHz and 16.0 GB RAM. In GMRES implementation, the library *FMMLIB3D* by Gimbutas and Greengard [15] (github.com/zgimbu-tas/fmmlib3d) is called to conduct the fast matrix-vector product. To compare the computational cost, we measure how the CPU time required to calculate the electrostatic interaction scales with the number of particles, N_p, and the number of patches per particle, n. Fig. 3(a) plots the average CPU times of each GMRES iteration with a group of particles arranged in a row. The number of surface patches for each particles is $n = 392$, and the surface-to-surface distance between adjacent particles is $d = 0.2R$. For each case, ten individual runs were performed to obtain the average CPU time. The standard deviations are shown as the error bars. Some error bars are not visible because they are smaller than the symbol size. A quadratic dependence of the CPU time on the particle number N_p is observed when only using GMRES, while the computational time scales as $N_p^{1.333}$ if FMM is employed. Fig. 3(b) shows the CPU time to calculate the electrostatic interaction between two spheres with the surface-to-surface distance $d = 0.5R$. The quadratic scaling still holds for GMRES alone. When FMM is incorporated, the cost scaling reduces to $n^{1.564}$ as the number of surface patches on each particle increases. Thus, the calculation efficiency is significantly improved. For a more sophisticated implementation of FMM that optimizes the octree structure, a linear or nearly linear growth of the calculation cost can be expected [4,32]. Note that, in this analysis, the computational time is not simply a function of the matrix size $N = n \times N_p$. The convergence time is longer for patches closer to each other as their couplings are stronger. So the computational time for one particle discretized into 100 surface patches is different from that for 10 particles with each one covered by 10 surface patches.

2.2. Particle transport

The position and orientation of an ellipsoidal particle can be described by three coordinate frames, which can be referred to as the inertial frame $\mathbf{x}^{(in)} = [x^{(in)}, y^{(in)}, z^{(in)}]^T$, the co-moving frame $\mathbf{x}^{(cm)} = [x^{(cm)}, y^{(cm)}, z^{(cm)}]^T$, and the particle frame $\mathbf{x}^{(p)} = [x^{(p)}, y^{(p)}, z^{(p)}]^T$, as shown in Fig. 4. The co-moving frame translates with the particle and its origin is fixed at the particle centroid. The axes of the particle frame always coincide with the semi-axes of the ellipsoid, so the particle frame records both the translational and rotational movements of the particle. For a point in the inertial frame, its generalized position vector $\mathbf{X}^{(in)} = [x^{(in)}, y^{(in)}, z^{(in)}, 1]^T$ can be transformed to the co-moving frame by $\mathbf{X}^{(cm)} = \mathcal{T}\mathbf{X}^{(in)}$. Here, the translation matrix $\mathcal{T}$ is defined as

$$\mathcal{T} = \begin{bmatrix} 1 & 0 & 0 & -x_p^{(in)} \\ 0 & 1 & 0 & -y_p^{(in)} \\ 0 & 0 & 1 & -z_p^{(in)} \\ 0 & 0 & 0 & 1 \end{bmatrix},$$ (15)

with $(x_p^{(in)}, y_p^{(in)}, z_p^{(in)})$ being the coordinates of the particle centroid in the inertial frame. The transformation between the co-moving frame and the particle frame is $\mathbf{X}^{(p)} = \mathcal{R}\mathbf{X}^{(cm)}$. The rotation matrix $\mathcal{R}$ can be expressed by the Euler angles
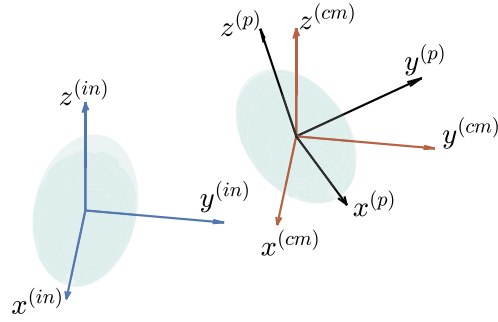
Fig. 4. Schematic of different coordinate frames. The inertial, co-moving and particle frames are colored in blue, red and black, respectively. (For interpretation of the colors in the figure(s), the reader is referred to the web version of this article.)

(ϕ, θ, ψ) or quaternions $(\varepsilon_1, \varepsilon_2, \varepsilon_3, \eta)$. In this study, we follow the work by Chesnutt and Marshall [12] and express $\mathcal{R}$ in the form of quaternions

$$
\mathcal{R} = \begin{bmatrix} 1 - 2(\varepsilon_2^2 + \varepsilon_3^2) & 2(\varepsilon_1\varepsilon_2 + \varepsilon_3\eta) & 2(\varepsilon_1\varepsilon_3 - \varepsilon_2\eta) & 0 \\ 2(\varepsilon_2\varepsilon_1 - \varepsilon_3\eta) & 1 - 2(\varepsilon_3^2 + \varepsilon_1^2) & 2(\varepsilon_2\varepsilon_3 + \varepsilon_1\eta) & 0 \\ 2(\varepsilon_3\varepsilon_1 + \varepsilon_2\eta) & 2(\varepsilon_3\varepsilon_2 - \varepsilon_1\eta) & 1 - 2(\varepsilon_1^2 + \varepsilon_2^2) & 0 \\ 0 & 0 & 0 & 1 \end{bmatrix}.
\tag{16}
$$

The initial values of quaternions are given by

$$
\varepsilon_1 = \cos\frac{\phi - \psi}{2}\sin\frac{\theta}{2}, \ \varepsilon_2 = \sin\frac{\phi - \psi}{2}\sin\frac{\theta}{2}, \ \varepsilon_3 = \sin\frac{\phi + \psi}{2}\cos\frac{\theta}{2}, \ \eta = \cos\frac{\phi + \psi}{2}\cos\frac{\theta}{2}.
\tag{17}
$$

Then quaternions are evolved by

$$
\begin{bmatrix} d\varepsilon_1/dt \\ d\varepsilon_2/dt \\ d\varepsilon_3/dt \\ d\eta/dt \end{bmatrix} = \frac{1}{2}\begin{bmatrix} \eta\Omega_x^{(p)} - \varepsilon_3\Omega_y^{(p)} + \varepsilon_2\Omega_z^{(p)} \\ \varepsilon_3\Omega_x^{(p)} + \eta\Omega_y^{(p)} - \varepsilon_1\Omega_z^{(p)} \\ -\varepsilon_2\Omega_x^{(p)} + \varepsilon_1\Omega_y^{(p)} + \eta\Omega_z^{(p)} \\ -\varepsilon_1\Omega_x^{(p)} - \varepsilon_2\Omega_y^{(p)} - \varepsilon_3\Omega_z^{(p)} \end{bmatrix}.
\tag{18}
$$

Here $\Omega_x^{(p)}$, $\Omega_y^{(p)}$ and $\Omega_z^{(p)}$ are the components of particle's rotation rate in the particle frame.

The discrete element method (DEM) is employed to evolve particle movements. The governing equations of the linear and angular momentum are given as

$$
m\frac{d\mathbf{v}_i^{(in)}}{dt} = \mathbf{F}_{E,i}^{(in)} + \sum_{j \neq i} \mathbf{F}_{C,j \to i}^{(in)},
\tag{19}
$$

$$
I_x^{(p)}\frac{d\Omega_{x,i}^{(p)}}{dt} - \Omega_{y,i}^{(p)}\Omega_{z,i}^{(p)}(I_y^{(p)} - I_z^{(p)}) = M_{E,i,x}^{(p)} + \sum_{j \neq i} M_{C,j \to i,x}^{(p)},
\tag{20a}
$$

$$
I_y^{(p)}\frac{d\Omega_{y,i}^{(p)}}{dt} - \Omega_{z,i}^{(p)}\Omega_{x,i}^{(p)}(I_z^{(p)} - I_x^{(p)}) = M_{E,i,y}^{(p)} + \sum_{j \neq i} M_{C,j \to i,y}^{(p)},
\tag{20b}
$$

$$
I_z^{(p)}\frac{d\Omega_{z,i}^{(p)}}{dt} - \Omega_{x,i}^{(p)}\Omega_{y,i}^{(p)}(I_x^{(p)} - I_y^{(p)}) = M_{E,i,z}^{(p)} + \sum_{j \neq i} M_{C,j \to i,z}^{(p)}.
\tag{20c}
$$

Here, $\mathbf{v}_i^{(in)}$ and $\mathbf{\Omega}_i^{(p)} = [\Omega_{x,i}^{(p)}, \Omega_{y,i}^{(p)}, \Omega_{z,i}^{(p)}]^T$ are the velocity and the rotation rate of particle i. m is the particle mass, $\mathbf{I}^{(p)} = [I_x^{(p)}, I_y^{(p)}, I_z^{(p)}]^T$ is the moment of inertia. For an ellipsoidal particle with three semi-axes length of a, b, and c, the three components of its moment of inertia are $I_x^{(p)} = m(b^2 + c^2)/5$, $I_y^{(p)} = m(c^2 + a^2)/5$ and $I_z^{(p)} = m(a^2 + b^2)/5$. $\mathbf{F}_{E,i}^{(in)}$ and $\mathbf{M}_{E,i}^{(p)}$ are the electrostatic force and torque exerted on particle i. $\mathbf{F}_{C,j \to i}^{(in)}$ and $\mathbf{M}_{C,j \to i}^{(p)} = [M_{C,j \to i,x}^{(p)}, M_{C,j \to i,y}^{(p)}, M_{C,j \to i,z}^{(p)}]^T$ are the contact force and torque acting on particle i by particle j.
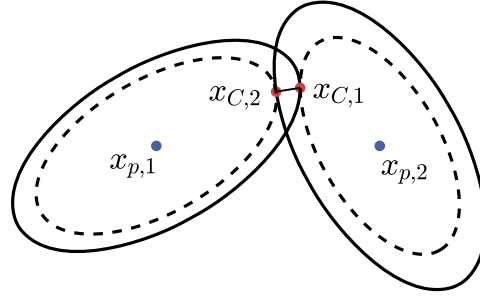
Fig. 5. Schematic of collision detection. Particle surfaces are shown as solid profiles. The innermost level surfaces are denoted by dashed lines.

2.3. Collision between ellipsoidal particles

2.3.1. Collision detection

In the particle frame of the i-th particle, every point on the surface satisfies the equation

$$\mathbf{X}^{(p)T} \mathcal{Q}_i^{(p)} \mathbf{X}^{(p)} = 0. \tag{21}$$

Here, the surface point position follows $\mathbf{X}^{(p)} = [x^{(p)}, y^{(p)}, z^{(p)}, 1]^T$, and the ellipsoid's characteristic matrix $\mathcal{Q}_i^{(p)}$ is expressed as

$$\mathcal{Q}_i^{(p)} = \begin{bmatrix} 1/a^2 & 0 & 0 & 0 \\ 0 & 1/b^2 & 0 & 0 \\ 0 & 0 & 1/c^2 & 0 \\ 0 & 0 & 0 & -1 \end{bmatrix}. \tag{22}$$

To relate the particle frame to the inertial frame, Eq. (21) can also be written as

$$\mathbf{X}^{(in)T} \mathcal{Q}_i^{(in)} \mathbf{X}^{(in)} = 0 \tag{23}$$

where $\mathbf{X}^{(p)} = \mathcal{R}\mathcal{T}\mathbf{X}^{(in)}$, and $\mathcal{Q}_i^{(in)} = \mathcal{T}^T \mathcal{R}^T \mathcal{Q}_i^{(p)} \mathcal{R}\mathcal{T}$ is a 4×4 characteristic matrix of the ith ellipsoid in the inertial frame.

The collision point between two ellipsoids can be detected if a non-zero solution of $\mathbf{X}^{(in)}$ satisfies Eq. (23) for two different characteristic matrices $\mathcal{Q}_1^{(in)}$ and $\mathcal{Q}_2^{(in)}$ at the same time. In practice, instead of solving two equations, we multiply Eq. (23) of ellipsoid 1 by λ and subtract that of ellipsoid 2, which then yields:

$$\mathbf{X}^{(in)T} (\lambda \mathcal{Q}_1^{(in)} - \mathcal{Q}_2^{(in)}) \mathbf{X}^{(in)} = 0. \tag{24}$$

It has been shown that, if a family of non-trivial solutions $\mathbf{X}^{(in)}$ exist, $\mathcal{Q}_1^{(in)-1} \mathcal{Q}_2^{(in)}$ should be singular, since $\mathcal{Q}_1^{(in)}$ is invertible. In the simulation, we check the eigenvalues of $\mathcal{Q}_1^{(in)-1} \mathcal{Q}_2^{(in)}$ for two adjacent ellipsoids. If the two eigenvalues are complex conjugates, these two ellipsoids intersect [1].

2.3.2. Contact point identification

When two ellipsoids intersect, the contact point is identified by using the method of level surfaces. In particular, Eq. (23) can be interpreted as level surfaces $P_i(\mathbf{x}^{(in)}) = \alpha$. In Fig. 5, $\alpha = 0$ for both solid level surfaces and $\alpha < 0$ for both dashed level surfaces. $P_i(\mathbf{x}^{(in)})$ is essentially the quadratic form of Eq. (23), which can be explicitly written as:

$$P_i(\mathbf{x}^{(in)}) = \mathbf{x}^{(in)T} \mathcal{S}_i^{(in)} \mathbf{x}^{(in)} + \mathbf{b}_i^{(in)T} \mathbf{x}^{(in)} + c_i^{(in)} = 0. \tag{25}$$

Here, $\mathcal{S}_i^{(in)}$, $\mathbf{b}_i^{(in)}$ and $c_i^{(in)}$ represent three components of $\mathcal{Q}_i^{(in)}$

$$\mathcal{S}_i^{(in)} = \begin{bmatrix} q_{11}^{(in)} & q_{12}^{(in)} & q_{13}^{(in)} \\ q_{12}^{(in)} & q_{22}^{(in)} & q_{23}^{(in)} \\ q_{13}^{(in)} & q_{23}^{(in)} & q_{33}^{(in)} \end{bmatrix} \tag{26}$$

$$\mathbf{b}_i^{(in)} = 2[q_{14}^{(in)}, q_{24}^{(in)}, q_{34}^{(in)}]^T, \tag{27}$$

$$c_i^{(in)} = q_{44}^{(in)}. \tag{28}$$

For two overlapping ellipsoids, there will be two contact points, each of which is defined as the tangent of one ellipsoid's surface on the innermost level surface of the other ellipsoid. Specifically, in Fig. 5, $x_{C,1}$ can be solved based on $P_1(x_{C,1}) = 0$

and $P_2(x_{C,1}) = \alpha_1$, while $x_{C,2}$ can be determined from $P_2(x_{C,2}) = 0$ and $P_1(x_{C,2}) = \alpha_2$. Then finding the two contact points becomes finding the local minimum of functions of P_2 and P_1 subject to equality constraints of $P_1(x_{C,1}) = 0$ and $P_2(x_{C,2}) = 0$, which can be determined using the Lagrangian multiplier. Here, we only solve one contact point at $\mathbf{x}_{C,1}^{(in)}$ as an example. The steps to solve the other one is identical. The Lagrangian function is defined as:

$$\mathcal{L}(\mathbf{x}^{(in)}) = P_2(\mathbf{x}^{(in)}) + \tau P_1(\mathbf{x}^{(in)}) \tag{29}$$

where τ is the Lagrangian multiplier. For optimization, the contact point $\mathbf{x}_{C,1}^{(in)}$ is given by

$$\mathbf{x}_{C,1}^{(in)} = -\frac{1}{2}(\mathcal{S}_2^{(in)} + \tau \mathcal{S}_1^{(in)})^{-1}(\mathbf{b}_2^{(in)} + \tau \mathbf{b}_1^{(in)}) = \frac{1}{\Phi(\tau)}\mathbf{y}(\tau), \tag{30}$$

where $\Phi(\tau) = det(\mathcal{S}_2^{(in)} + \tau \mathcal{S}_1^{(in)})$ is the determinant of $(\mathcal{S}_2^{(in)} + \tau \mathcal{S}_1^{(in)})$. τ can be obtained from the following the sixth-order polynomial

$$\mathbf{y}(\tau)^T \mathcal{S}_1^{(in)} \mathbf{y}(\tau) + \Phi(\tau)\mathbf{b}_1^{(in)^T}\mathbf{y}(\tau)^T + \Phi^2(\tau)c_1 = 0. \tag{31}$$

Numerically, Eq. (31) is calculated first to obtain τ, which typically have multiple solutions. Each one of the solutions leads to a different $\mathbf{x}_{C,1}^{(in)}$, but only the one with the smallest α_1 in the level surface equation ($P_2(x_{C,1}) = \alpha_1$) will be selected as the final solution (for details, see [12]).

2.3.3. Contact forces and torques

Once the positions of the two contact points are identified, one can determine the normal overlap $\delta_N = \left|\mathbf{x}_{C,i}^{(in)} - \mathbf{x}_{C,j}^{(in)}\right|$ between these two points and their relative velocity ($\mathbf{v}_{rel}^{(in)}$). Based on these two variables, the contact force $\mathbf{F}_{C,j \to i}^{(in)}$ can be calculated by following the Hertzian contact model [36].

$$\mathbf{F}_{C,j \to i}^{(in)} = (F_{ne} + F_{nd})\mathbf{n} + F_t \mathbf{t} \tag{32}$$

where $\mathbf{n}$ is the unit vector along the outward normal direction at the contact point given by

$$\mathbf{n}(\mathbf{x}_{C,i}^{(in)}) = \nabla P_i(\mathbf{x}_{C,i}^{(in)})/\left|\nabla P_i(\mathbf{x}_{C,i}^{(in)})\right|, \tag{33}$$

and the tangent unit vector follows the direction of the tangential relative velocity ($\mathbf{v}_{rel,t}^{(in)}$) between two contact points:

$$\mathbf{t} = \mathbf{v}_{rel,t}^{(in)}/\left|\mathbf{v}_{rel,t}^{(in)}\right|. \tag{34}$$

$$\mathbf{v}_{rel,t}^{(in)} = (\mathbf{v}_{C,i}^{(in)} - \mathbf{v}_{C,j}^{(in)}) - (\mathbf{v}_{C,i}^{(in)} - \mathbf{v}_{C,j}^{(in)}) \cdot \mathbf{n}. \tag{35}$$

For the contact force, the normal component consists of two terms, i.e., the normal elastic force F_{ne} and the normal dissipative force F_{nd}. The normal elastic force can be expressed as

$$F_{ne} = -k_N \delta_N. \tag{36}$$

In addition to the normal overlap δ_N, the elastic stiffness k_N can be expressed as $k_N = \frac{4}{3}E\sqrt{R\delta_N}$, which depends on the reduced radius $R = (K_{C,i} + K_{C,j})^{-1}$ by averaging the local curvatures at two contact points. In particular, the local curvature K_i is given by

$$K_i = \frac{h^3}{2}[\frac{1}{a^2b^2}(\frac{(x_i^{(p)})^2}{a^2} + \frac{(y_i^{(p)})^2}{b^2}) + \frac{1}{b^2c^2}(\frac{(y_i^{(p)})^2}{b^2} + \frac{(z_i^{(p)})^2}{c^2}) + \frac{1}{c^2a^2}(\frac{(z_i^{(p)})^2}{c^2} + \frac{(x_i^{(p)})^2}{a^2})], \tag{37a}$$

$$h = [(x_i^{(p)})^2/a^4 + (y_i^{(p)})^2/b^4 + (z_i^{(p)})^2/c^4]^{-1/2}. \tag{37b}$$

The effective elastic modulus E is defined as

$$\frac{1}{E} = \frac{1-\nu_i^2}{E_i} + \frac{1-\nu_j^2}{E_j}, \tag{38}$$

where E_i and ν_i are the elastic modulus and Poisson ratio of particle i.

The other normal force component is contributed by the dissipation, which is proportional to the normal relative velocity $F_{nd} = -\eta_N \mathbf{v}_{rel} \cdot \mathbf{n}$. The normal dissipation coefficient is defined as $\eta_N = \alpha_N(mk_N)^{1/2}$. Here, m is the particle mass, α_N is related to the coefficient of restitution e [36]. The tangential force is calculated based on the static friction model and expressed as

$$F_t = -\mu_F\left|F_n\right|, \tag{39}$$
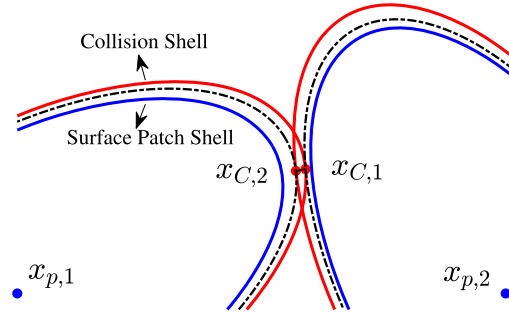
Fig. 6. Schematic of the double-shell model. The collision shell is plotted as red profiles and the surface patch shell is shown as blue profiles. The level surfaces are denoted by the dash dot lines.

where the friction coefficient μ_F is set as 0.3, which provides good agreement with experimental measurements [51]. Once the full contact force $\mathbf{F}_{C,j \to i}^{(in)}$ is obtained, the corresponding rotation torque is computed by

$$\mathbf{M}_{C,j \to i}^{(in)} = \mathbf{r}_{C,ij}^{(in)} \times \mathbf{F}_{C,j \to i}^{(in)}, \tag{40}$$

where $\mathbf{r}_{C,i}^{(in)} = \mathbf{x}_{C,i}^{(in)} - \mathbf{x}_{p,i}^{(in)}$ is the position vector, pointing from the ellipsoid centroid $\mathbf{x}_{p,i}^{(in)}$ to the contact point $\mathbf{x}_{C,i}^{(in)}$.

2.3.4. Double shell model

Detecting the collision and calculating the contact force require a small overlap between two particles. However, no overlap is allowed in the BEM model because, if surface patches m and n coincide, the Green function $\mathcal{I}_{mn}$ defined in Eq. (12) becomes singular. In this study, we use the *double-shell model* to address this problem. As shown in Fig. 6, two different shells are used to calculate the electrostatic interaction and the contact force, respectively. The original ellipsoidal surface is the surface patch shell (blue line) on which the discretized surface patches reside, while a slightly larger parallel shell is used to calculate the contact interactions (red line). The thickness of the *buffer layer* in between is defined as δ_{bl}. The characteristic matrix of the collision shell in Eq. (22) then becomes

$$\mathcal{Q}_i^{(p)} = \begin{bmatrix} 1/(a+\delta_{bl})^2 & 0 & 0 & 0 \\ 0 & 1/(b+\delta_{bl})^2 & 0 & 0 \\ 0 & 0 & 1/(c+\delta_{bl})^2 & 0 \\ 0 & 0 & 0 & -1 \end{bmatrix}. \tag{41}$$

It should be noted that, the buffer layer should be thin enough so that the error introduced by the two shells not coinciding with each other is negligible. How to select δ_{bl} will be further discussed in Section 3.3.1.

2.4. Simulation acceleration using the reduced particle stiffness

For simulating particle motion, the smallest time scale is the collision time scale τ_C, which scales as $\tau_C \sim [m^2/(E^2 R v_0)]^{1/5} \sim [\rho_p^2/(E^2 v_0)]^{1/5} R$. In order to accurately resolve the collision, a fine time step $\Delta t_C = f_C \tau_C$ is required where f_C is much smaller than unity [30,29]. For small solid particles, the calculation becomes extremely expensive. To address this challenge, the elastic modulus is often reduced to soften the particle numerically so a larger time step Δt_C is sufficient [6,11,45]. To avoid any unphysical effects brought by the reduced stiffness, other forces acting on the particles should also be modified accordingly [18,52].

Here, the linear momentum equation is modified from Eq. (19) for a pair of charged particles colliding head on.

$$m \frac{d\mathbf{v}}{dt} = -(k_N \delta_N + \eta_N v_{rel,n})\mathbf{n} + \mathbf{F}_E. \tag{42}$$

To nondimensionalize this equation, we define the dimensionless velocity $\hat{\mathbf{v}}$ and overlap $\hat{\delta}_N$ as $\hat{\mathbf{v}} = \mathbf{v}/v_0$ and $\hat{\delta}_N = \delta_N/\delta_0$, respectively. Here, the approaching velocity v_0 between two colliding particles is chosen as the characteristic velocity, while the characteristic overlap is given by $\delta_0 = [mv_0^2/(ER^{1/2})]^{2/5}$. Finally, the nondimensionalized Eq. (42) becomes

$$\frac{d\hat{\mathbf{v}}}{d\hat{t}} + \frac{4}{3}\hat{\delta}_N^{3/2}\mathbf{n} + \frac{2}{\sqrt{3}}\alpha_N \hat{\delta}_N^{1/4}\hat{v}_{rel,n}\mathbf{n} = \left(\frac{1}{m^3 v_0^6 E^2 R}\right)^{1/5} \mathbf{F}_E. \tag{43}$$

where the dimensionless electrostatic force $\hat{\mathbf{F}}_E = \mathbf{F}_E(m^3 v_0^6 E^2 R)^{-1/5}$ scales with $E^{-2/5}$. As the stiffness is reduced for contact force calculation, the dimensional electrostatic force should be corrected accordingly:
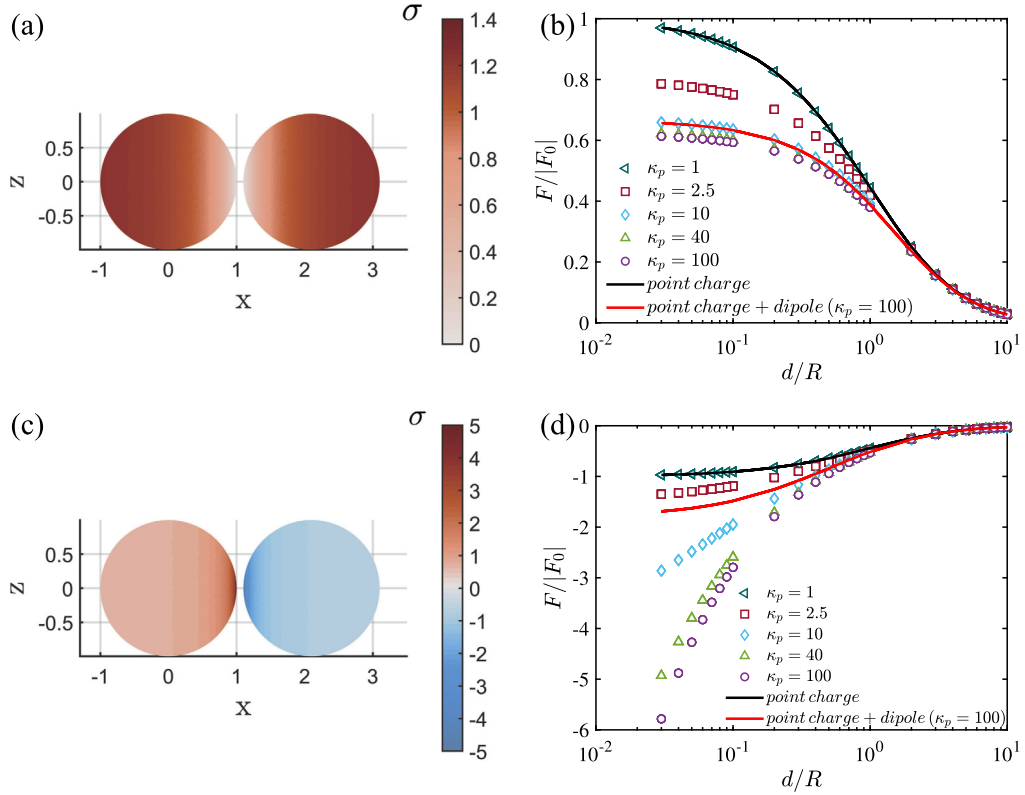
Fig. 7. Surface charge density of two close particles with $\kappa_p = 10$ and $d/R = 0.1$ with the nominal charge density (a) $\sigma_{f,1} = \sigma_{f,2} = 1$ and (c) $\sigma_{f,1} = 1, \sigma_{f,2} = -1$. (b), (d): Dependence of the normalized electrostatic force $F/|F_0|$ on the normalized surface-to-surface separation distance d/R between two dielectric particles corresponding to (a) and (c).

$$\mathbf{F}_{E,R} = \left(\frac{E_R}{E_O}\right)^{2/5} \mathbf{F}_{E,O} = \chi^{2/5} \mathbf{F}_{E,O}. \tag{44}$$

Here, the subscripts O and R denote variables for particles with the original or reduced stiffness, respectively. $\chi = E_R/E_O$ is the stiffness ratio. The electrostatic torque is also adjusted in a similar way. It is worth noting that the electrostatic force and torque are *only* modified in a collision process. When particles are not in contact, their dynamics are evolved using the original values of $F_{E,O}$ and $M_{E,O}$.

3. Results and discussions

3.1. Electrostatic force between charged spheres

To validate the BEM method and use it to evaluate other simplified models, we compute the electrostatic force between two dielectric spheres that are very close to each other with the shortest distance in between d. If the two spheres are equally charged with charge density $\sigma_{f,1} = 1$ (left) and $\sigma_{f,2} = 1$ (right), the typical surface charge distribution is displayed in Fig. 7(a). Bound charge of the opposite sign will be induced on the near side, while the same-sign charge will be induced on the far side. For this particular case, because the entire problem is symmetric, the surface charges approach zero on the near side and exceed the initial charge density on the far side, which leads to the polarization. This polarization will weaken the repulsive force between the two spheres because it essentially pushes most charges to the far side of each particle and increases the distance in between. As κ_p increases, this polarization grows and the repulsive force drops even further, but the effect of the particle polarization is found to saturate when κ_p is large (e.g., $\kappa_p = 40$ and $\kappa_p = 100$ in Fig. 7(b)). Further increasing κ_p does not weaken the repulsive force anymore.

If we assume that particles interact with each other only through their point charges and dipoles, the problem can be directly solved by expressing the electrostatic force acting on the ith particle located at $\mathbf{x}_i$ as

$$\mathbf{F}_{E,i} = q_i \mathbf{E}(\mathbf{x}_i) + \mathbf{p}_i \cdot \nabla \mathbf{E}(\mathbf{x}_i), \tag{45}$$

where q_i is the net charge on the particle, $\mathbf{p}_i$ is its dipole moment. The electric field at the particle position is

$$\mathbf{E}(\mathbf{x}_i) = \sum_{j \neq i} \left[\frac{q_j \mathbf{r}_{ij}}{4\pi \varepsilon_0 r_{ij}^3} - \nabla \left(\frac{\mathbf{p}_j \cdot \mathbf{r}_{ij}}{4\pi \varepsilon_0 r_{ij}^3} \right) \right]. \tag{46}$$

Here, the induced dipole is assumed to depend linearly on the local field strength as

$$\mathbf{p}_i = 4\pi \varepsilon_0 K_{CM} r_p^3 \mathbf{E}(\mathbf{x}_i), \tag{47}$$

where the *Clausius-Mossotti* function K_{CM} equals

$$K_{CM} = \frac{\kappa_p - \kappa_0}{\kappa_p + 2\kappa_0}. \tag{48}$$

The electrostatic force has been divided into the contributions from the point charge (monopole) and dipole-dipole interactions. If one considers only the point charge, the problem simplifies to the interaction between two point charges located at the center of mass of the two spheres. If the two spheres almost touch each other ($d = 0$), the associated Coulomb force in this case follows $F_0 = \pi R^2 \sigma_{f,1} \sigma_{f,2} / \varepsilon_0$, which can be used as the characteristic Coulomb force for normalization.

The normalized electrostatic force $F/|F_0|$ versus d is shown in Fig. 7(b) as the black line, and it coincides with the BEM result of $\kappa_p = 1$, where the spheres have no polarization. This implies that, if the effect of the induced surface charge is neglected, the electrostatic interaction will reduce to the simple Coulomb interaction.

When $\kappa_p > 1$, spheres become polarizable. The bound charge σ_b is induced as two spheres approach each other. The resulting repulsive force is weakened and deviates from the Coulomb force when $d/R \leq 2$. This deviation grows as κ_p increases. To account for this change, the dipole interaction is added and the problem becomes coupled, as indicated by Eq. (46) and Eq. (47). To solve this coupled problem, we assume the initial dipole $\mathbf{p}_i^{(0)} = \mathbf{0}$ and compute the field strength $\mathbf{E}^{(0)}(\mathbf{x}_i)$. Eq. (46) and Eq. (47) are iterated until $\mathbf{p}_i$ converges, from which the electrostatic force is acquired based on Eq. (45).

The electrostatic force predicted by the model adding point charge and dipole contributions (monopole-dipole model) is shown as the red line for $\kappa_p = 100$ in Fig. 7(b). In the dipole model, the polarization of the particle can be approximated by the relative separation of the positive and negative charges at the particle scale. For two equally charged dielectric spheres shown in Fig. 7(a), there is obvious particle-scale charge separation. Thus, the induced dipole model should provide reasonable estimation of the electrostatic force despite its simplified nature. As expected, adding the dipole interaction indeed captures the weakened electrostatic force compared with the point-charge model alone. Nevertheless, compared with the BEM prediction at $\kappa_p = 100$, the dipole model overpredicts the repulsive force because the bound charge density has a strong variation at a scale much smaller than the particle size, which cannot be captured by the monopole-dipole model.

This deviation between the simplified monopole-dipole model and the BEM result is more obvious for two oppositely charged spheres, as shown in Fig. 7(c). For this case, the initial charge densities of the two spheres are set as $\sigma_{f,1} = 1$ (left) and $\sigma_{f,2} = -1$ (right). The bound charge density becomes higher on the near side of each particle because of the electrostatic attraction by the other. The induced charge further enhances this attraction. As a result, the local charge density becomes much higher than the initial free charge density and thus drastically increases the attractive force between the two spheres (Fig. 7(d)). In contrast to large regions covered by induced charges (light red areas) for two equally charged spheres shown in Fig. 7(a), the induced charge is concentrated locally on the near side as shown in Fig. 7(c). Since the dipole model only captures the induced charge separation occurred at the particle scale, this is not surprising that the dipole model significantly underestimates the electrostatic attraction between the two spheres (red line in Fig. 7(d)). This result underlines the importance of including the multipole interaction for characterizing the attractive force between two oppositely-charged particles.

3.2. Electrostatic interaction on non-spherical particles

So far, computing the electrostatic interaction between two charged spheres helps to validate the force predicted by the BEM model. Since the advantage of the BEM model is its adaptability to almost any particle geometries, we intend to examine its performance for non-spherical particles. For this type of particles, in addition to the position, the orientation also matters even though the dielectric property of particle material could be homogeneous and isotropic. To characterize the evolution of orientation, one needs to include the calculation of torque. In this section, we focus on the modulation of the electrostatic interaction, including both force and torque, induced by the non-spherical particle geometry.

3.2.1. Electrostatic torque on an ellipsoidal particle

For a neutral dielectric ellipsoid placed in a uniform external field, the net electrostatic force remains zero. However, due to the geometry, there could be a non-uniform distribution of surface charges on the particle, and their interaction with the external field leads to a non-zero total electrostatic torque acting on the ellipsoid. For a neutral dielectric ellipsoid defined by $x^2/a^2 + y^2/b^2 + z^2/c^2 = 1$, the electrostatic torque $\mathbf{M}_E$ exerted by the external field $\mathbf{E}_{ext} = [E_x, E_y, E_z]$ is given by [23]

$$M_{E,x} = \frac{4\pi \varepsilon_0 abc}{3} \frac{(\tilde{\kappa} - 1)^2 (L_z - L_y) E_z E_y}{[1 + (\tilde{\kappa} - 1)L_z][1 + (\tilde{\kappa} - 1)L_y]}, \tag{49a}$$
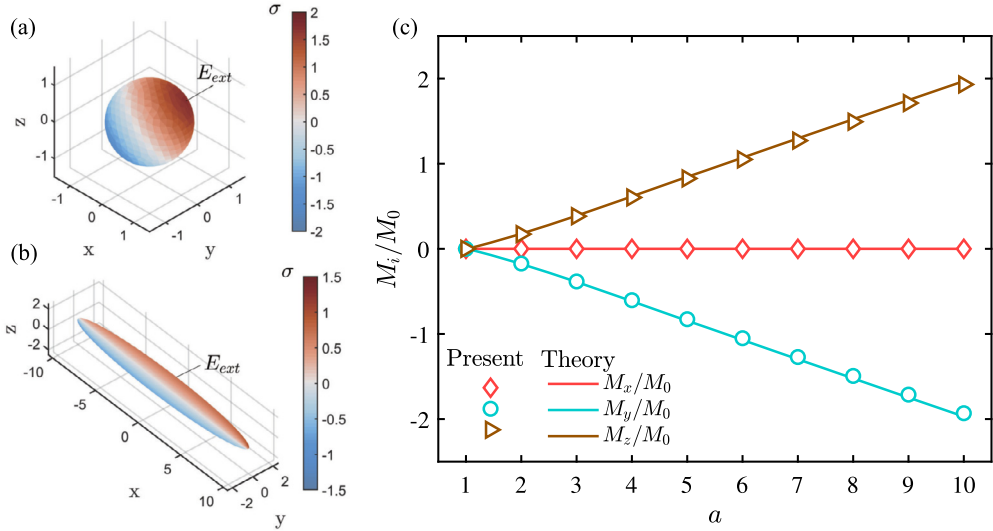
Fig. 8. Distribution of the nominal surface charge density for (a) $a = 1$ and (b) $a = 10$ under the external field. (c) Normalized torque acting on the dielectric ellipsoid exerted by the external field.

$$M_{E,y} = \frac{4\pi \varepsilon_0 abc}{3} \frac{(\tilde{\kappa} - 1)^2 (L_x - L_z) E_x E_z}{[1 + (\tilde{\kappa} - 1)L_x][1 + (\tilde{\kappa} - 1)L_z]}, \tag{49b}$$

$$M_{E,z} = \frac{4\pi \varepsilon_0 abc}{3} \frac{(\tilde{\kappa} - 1)^2 (L_y - L_x) E_y E_x}{[1 + (\tilde{\kappa} - 1)L_y][1 + (\tilde{\kappa} - 1)L_x]}. \tag{49c}$$

Here, κ_0 is the dielectric constant of the medium, $\tilde{\kappa} = \kappa_p/\kappa_0$ is the ratio of the dielectric constants. L_x, L_y, and L_z are the elliptical integrals, which are defined as

$$L_x = \frac{abc}{2} \int_0^\infty \frac{ds}{(s + a^2)R_s}, \tag{50a}$$

$$L_y = \frac{abc}{2} \int_0^\infty \frac{ds}{(s + b^2)R_s}, \tag{50b}$$

$$L_z = \frac{abc}{2} \int_0^\infty \frac{ds}{(s + c^2)R_s}, \tag{50c}$$

with $R_s = [(s + a^2)(s + b^2)(s + c^2)]^{1/2}$.

The dielectric constant of the particle and the medium is $\kappa_p = 2.5$ and $\kappa_0 = 1$. The particle is assumed to be prolate spheroids with the length of the two semi-minor axes (y and z axes) fixed at $b = c = 1$ and the length a of the semi-major axis (x axis) ranging from 1 to 10. The external field is set as $\mathbf{E} = E_0[1, 1, 1]/\sqrt{3}$, which is at a constant angle with all three major axes.

For $a = 1$, the ellipsoid reduces to a sphere, and the electrostatic torque becomes zero, as expected, because the induced charge on the sphere is symmetric about the direction of the external field (Fig. 8(a)). When summing over the whole spherical surface, the torque exerted on each patch cancels out. However, as the aspect ratio increases, if the direction of the external electric field does not align with any of the three axes of the particle body of rotation, the induced charge is no longer symmetric about the direction of the external field (Fig. 8(b)). Integrating over the ellipsoidal surface then yields a non-zero net torque. This torque will continue to rotate the ellipsoid until the induced surface charge becomes symmetric about the direction of the electric field again.

Fig. 8(c) compares the three components of the electrostatic torque given by Eq. 49 and normalized by $M_0 = 4\pi \varepsilon_0 b^3 E_0^2/3$ for this particle with aspect ratio ranging from 1 to 10. The torque along the x-axis is zero for all aspect ratios because rotating about the x-axis does not change the charge distribution and thus cannot serve to reduce the asymmetry of the induced charges. For the other two directions, the markers for the BEM calculations collapse on to the theoretical curves, which again validates the BEM method and shows its applicability on non-spherical geometries. As a increases, more patches are required to discretize the ellipsoidal surface and to keep the relative error within 2% compared to the theoretical predictions.
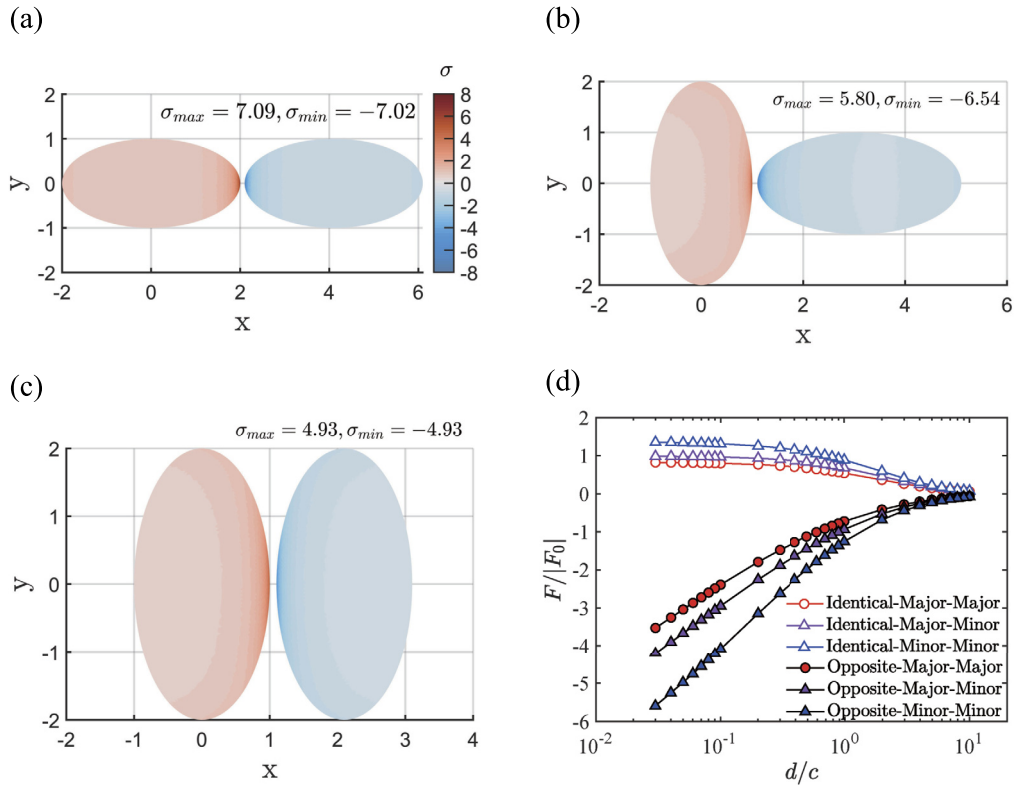
Fig. 9. The nominal surface charge distribution of two ellipsoids approaching each other (a) both along the major axis, (b) along the major and minor axis respectively and (c) both along the minor axis with $\kappa_p = 10$ and $d/R = 0.1$. The color bar in (a) also applies to (b) and (c). (d) The normalized electrostatic force $F/|F_0|$ between two dielectric ellipsoids with the nominal charge density $\sigma_{f,1} = 1$ and $\sigma_{f,2} = -1$.

3.2.2. Electrostatic force between two charged dielectric ellipsoids

As discussed in Section 3.1, due to the symmetry, the electrostatic force between two spheres does not rely on the direction along which two particles approach each other. But for ellipsoidal particles, the particle orientation could modify the amount of induced surface charges, thereby affecting the electrostatic force. Without loss of generality, three typical configurations are chosen here for two oppositely-charged prolate spheroid particles ($a = 2$ and $b = c = 1$) approaching each other (i) both along the major axis (head-to-tail configuration in Fig. 9(a)), (ii) along the major and minor axis, respectively (perpendicular configuration in Fig. 9(b)), and (iii) both along the minor axis (side-by-side configuration in Fig. 9(c)). Here, the dielectric constant is kept at $\kappa_p = 10$ and the dimensionless free charge density is $\sigma_{f,1} = 1$ (left) and $\sigma_{f,2} = -1$ (right), respectively.

The particle separation d is the same for all three configurations. But the maximum local induced charge density σ_{max} on the surface seems to be very sensitive to the particle orientations. The largest σ_{max} exceeds 7 (as shown by the upper limit of the color bar) when two ellipsoids arrange in the head-to-tail configuration (panel (a)), while σ_{max} drops to 5 in the side-by-side configuration (panel (c)). This suggests that the induced charge density is sensitive not only to the separation between two particles but also to the local geometric curvature. This can be attributed to the short-range nature of the induced higher-order multipoles. High-curvature tips tend to force the charges to focus more at the points that are close to the opposing particle.

However, a large σ_{max} does not necessarily lead to a large electrostatic force. In Fig. 9(d), the electrostatic force normalized by the characteristic Coulomb force $F_0 = \pi c^2 \sigma_{f,1} \sigma_{f,2}/\varepsilon_0$ is shown as a function of d/c for all three configurations. Among all three cases, the head-to-tail configuration with the largest σ_{max} has the weakest electrostatic attractive force, whereas the side-by-side configuration is the opposite. Although with a small surface charge density σ_{max}, its electrostatic force is the strongest. The same dependence is also observed for both identically charged particles $\sigma_{f,1} = 1$ (left) and $\sigma_{f,2} = 1$ (right) and oppositely charged particles $\sigma_{f,1} = 1$ (left) and $\sigma_{f,2} = -1$ (right). This trend simply implies that, even though the higher-order multipoles are very strong when particles are in close contact, their magnitudes decay rapidly as the surface-to-surface distance increases. Although the side-by-side configuration has a small σ_{max}, there is a much larger region in close contact between two particles. As a result, the contribution of all the induced surface charge is more significant and lead to a stronger electrostatic force.

Based on this observation, when forming an aggregate, particles could adjust both their positions and orientations to minimize the overall energy of the entire system. For identically charged particles, particles might organize in the head-to-
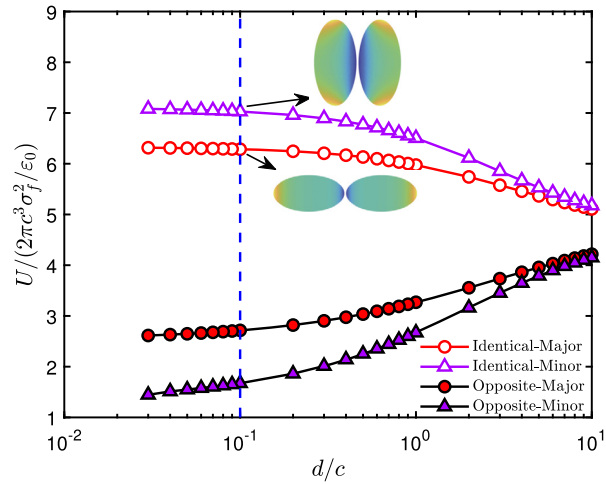
Fig. 10. Dimensionless electrostatic energy between two ellipsoids with $\kappa_p = 10$.

tail configuration to avoid strong repulsion. But for oppositely charged particles, the side-by-side configuration may be more favorable because of the stronger attraction as they both approach along the minor axis.

3.3. Dynamic simulation of particle-aggregate collision

In this section, we shift our attention from the discussion of the electrostatic interaction between two static charged particles to the dynamic simulations of a cluster of charged particles freely moving in 3D. To capture the collision in a cost-effective way, the reduced stiffness method, introduced in Section 2.4, is used. We will first discuss how to select the thickness of the buffer layer δ_{bl} and the reduced elastic modulus E_R without compromising accuracy. Then, two examples of the particle-aggregate collision are simulated to show the impact of the electrostatic interaction on the aggregation of charged dielectric non-spherical particles.

3.3.1. Buffer layer thickness

As introduced in Section 2.3.4, two shells are necessary to calculate the contact and electrostatic forces. The buffer layer in between should be as thin as possible so the numerical error is minimized. To identify how thin the buffer layer needs to be, we need to consider the electrostatic energy

$$U = \frac{1}{2} \int_S \sigma_f(\mathbf{r}) \psi(\mathbf{r}) dS \tag{51}$$

of two ellipsoids approaching each other. Here, $\psi(\mathbf{r})$ is the electric potential at $\mathbf{r}$. Fig. 10 plots the normalized U as a function of the normalized separation d/c.

In this study, the dielectric constant κ_p for both particles is kept at 10, which is comparable to that reported by Lee et al. [28]. As shown in Fig. 10, when two ellipsoids approach each other along the direction of the major/minor semi-axis, the corresponding U are shown as red/purple markers. It is found that U almost plateaus when the surface-to-surface distance satisfies $d \leq 0.1c$ (vertical blue dashed line in Fig. 10), which indicates that U does not change much if we set the buffer layer thickness $\delta_{bl} = 0.05c$ (c is the semi-minor axis). This layer thickness is therefore justified and will be used in the following dynamic simulations.

3.3.2. Reduced elastic modulus

In addition to the buffer layer, to accelerate the simulation, a reduced elastic modulus also needs to be selected. To simplify the problem, we investigate a basic case of the collision between two spheres. The simulation parameters are listed in Table 1. Two oppositely charged spheres located at $(0, 0, 0)$ and $(2.5R, 0, 0)$ are at rest initially. After the simulation begins, two spheres approach each other driven by the electrostatic attraction. When two particles collide, the time evolution of the overlap δ_N (Fig. 11(a)) and the normal relative velocity $v_{n,rel}$ (Fig. 11(b)) are shown as green markers. Since the original elastic modulus $E_O = 1 \times 10^9$ Pa is large, a fine time step $\Delta t_C = 1 \times 10^{-7}$ s is required to resolve the collision.

Additional simulations were performed with a reduced elastic modulus E_R for comparison. As introduced in Section 2.4, the original value of the electrostatic interaction is used before two particles collide, so the initial relative velocity is the same as the case using the original stiffness. Once two particles intersect, both the contact interaction and the electrostatic force are modified using the reduced elastic modulus E_R. For four values of E_R listed in Table 1, four different time steps are used, and their respective results are shown in Fig. 11(a) with different colors. For the softest case (dark blue), it can be seen
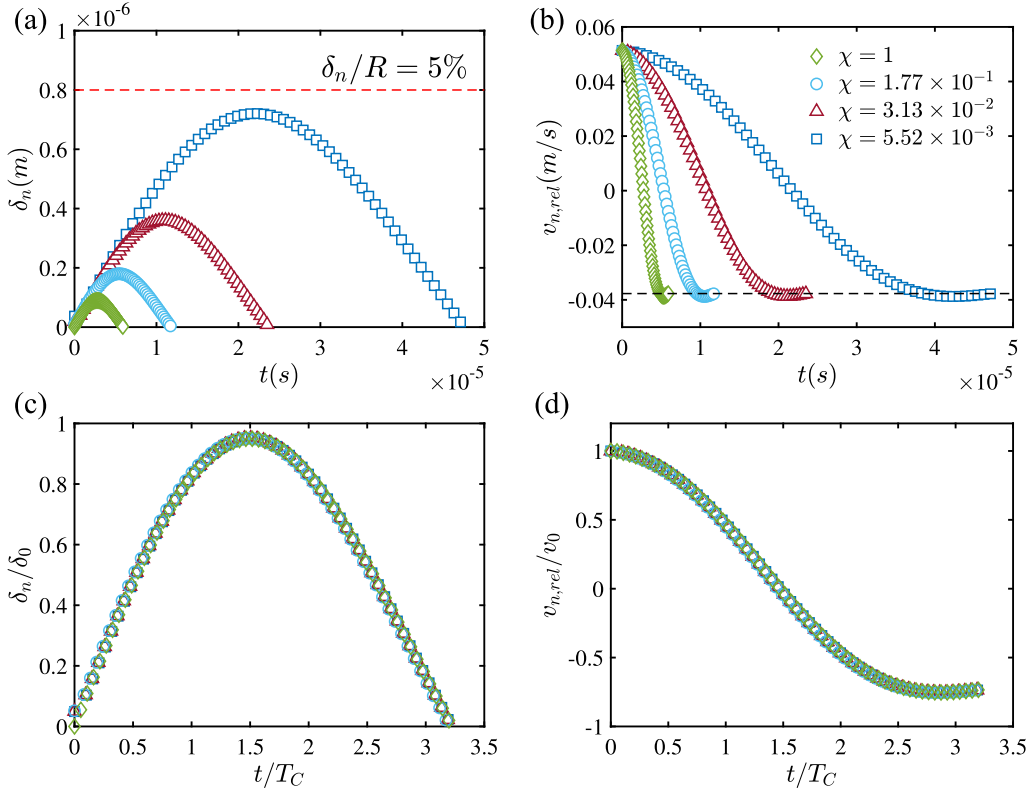
Fig. 11. (a) Dimensional normal overlap, (b) dimensional normal relative velocity, (c) dimensionless normal overlap and (d) dimensionless normal relative velocity between two oppositely charged particles in a head-on collision with modified electrostatic force.

Table 1
Simulation parameters for reduced stiffness tests.

| Parameters	Values	Units
Radius, R	100	μm
Buffer layer thickness, δ_{bl}	5	μm
Particle density, ρ_p	2500	kg/m^3
Free charge density, σ_f	± 6.4	μC/m^2
Original elastic modulus, E_0	1×10^9	Pa
Reduced ratio, χ	$1, 1.76 \times 10^{-1}, 3.13 \times 10^{-2}, 5.52 \times 10^{-3}$	–
Time step, Δt_C	$1 \times 10^{-7}, 2 \times 10^{-7}, 4 \times 10^{-7}, 8 \times 10^{-7}$	s
Dielectric constant of particle, κ_p	10	–
Dielectric constant of medium, κ_m	1	–
Restitution coefficient, e	0.7	–

that the collision duration, the maximum overlap, and the time step (gap between neighboring symbols) are the largest. But after being normalized by δ_0 (or v_0) and $T_C = \delta_0 / v_0$, the dimensionless curves of particles with different modulus coincide in Fig. 11 (c) and (d), which indicates that Eq. (43) provides identical results for different χ and reducing stiffness does not alter the collision outcomes.

Nevertheless, it does not mean that one can reduce the modulus unlimitedly. Since the characteristic overlap $\delta_0 \sim v_0^{4/5} E^{-2/5}$, increasing the incident velocity or reducing the elastic modulus will lead to a larger overlap. The largest overlap cannot exceed the buffer layer thickness, otherwise the overlapped surface mesh for electrostatic calculation will produce errors. To stay well below this limit, the maximum overlap $\delta_{N,max}$ is set to be smaller than 8% of $2\delta_{bl}$, which is equivalent to $\delta_{N,max}/R \lesssim 0.8\%$. To satisfy this condition for all particle velocities ($v_0 \leq 0.16$ m/s) considered in our simulations, the reduced ratio $\chi = 5.52 \times 10^{-3}$ is adopted, and the corresponding time step is chosen as $\Delta t_C = 8 \times 10^{-7}$ s. For future simulations that may target larger particle collision velocities, to ensure $\delta_{N,max} \sim \delta_0 < 2\delta_{bl}$, the elastic modulus should be chosen following Eq. (52).

$$E > \frac{m v_0^2}{(2\delta_{bl})^{5/2} R^{1/2}}. \tag{52}$$

Table 2
Simulation parameters of the particle-aggregate collision.

Parameters	Values	Units
Particle size, $a/b/c$	100/50/50	µm
Buffer layer thickness, δ_{bl}	2.5	µm
Particle density, ρ_p	2500	kg/m^3
Free charge density, σ_f	±5	µC/m^2
Original elastic modulus, E_0	1×10^9	Pa
Reduced ratio, χ	5.52×10^{-3}	–
Reduced elastic modulus, E_R	5.52×10^6	Pa
Dielectric constant of particle, κ_p	10	–
Dielectric constant of medium, κ_m	1	–
Restitution coefficient, e	0.7	–
Friction coefficient, μ_F	0.3	–
Incident velocity, v_0	0.02/0.16	m/s
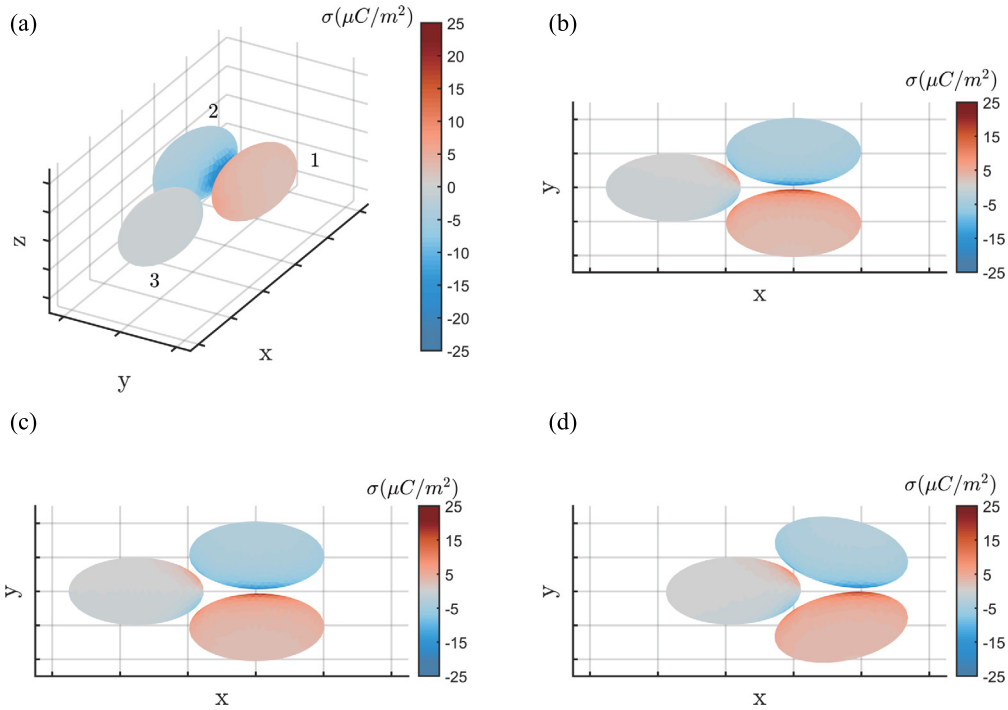
Fig. 12. Snapshots of the collision process between ellipsoid 3 and the side-by-side aggregate formed by ellipsoids 1 and 2 at (a) $t = 0.03$ ms, (b) $t = 1.11$ ms, (c) $t = 1.29$ ms and (d) $t = 9.6$ ms. The incident velocity of ellipsoid 3 is $v_0 = 0.02$ m/s along the x direction.

3.3.3. Particle-aggregate collision

In this section, we intend to demonstrate the simulation performance through two test cases of the collision between a neutral ellipsoidal particle with an aggregate formed by two oppositely charged ellipsoids. Different collision outcomes, such as sticking and fragmentation, indicate the role of electrostatic interactions in these collisions. The simulation parameters are listed in Table 2. The reduced elastic modulus E_R is used to accelerate the calculation (see Section 2.4).

Fig. 12 shows the four snapshots (a-d) of a typical collide-and-stick process. The initial configuration is displayed in Fig. 12(a). Particles 1 and 2, both of which have their semi-major axes oriented along the x-axis, are stuck together and form an agglomerate at rest. Particle 3 moves with an initial velocity of $v_0 = 0.02$ m/s also along the *x*-axis towards the gap between particle 1 and 2. Due to the induced surface charges, the electrostatic force acting on particle 3 becomes attractive when it is sufficiently close to the aggregate. This accounts for the acceleration of the incident particle as indicated by the gradual rise of the cyan curve in Fig. 13(a) and the decrease of the electrostatic energy in Fig. 13(c) between time instants of a and b.

When the first collision occurs at point b (marked by the sharp increase of δ_N for all three pairs in Fig. 12(b)), the kinetic energy of particle 3 is transferred to the aggregate, so the aggregate starts to translate along the x direction ($t \sim 1.1$ ms in Fig. 13(a)). Meanwhile, particle 1 and 2 begin to separate by rotating along opposite directions. Their kinetic energy continues to drop as separation has to overcome the electrostatic attraction, which leads to an increase of U between time instants b and c in Fig. 13(c). However, since the kinetic energy is not large enough for particles to escape, particle 1
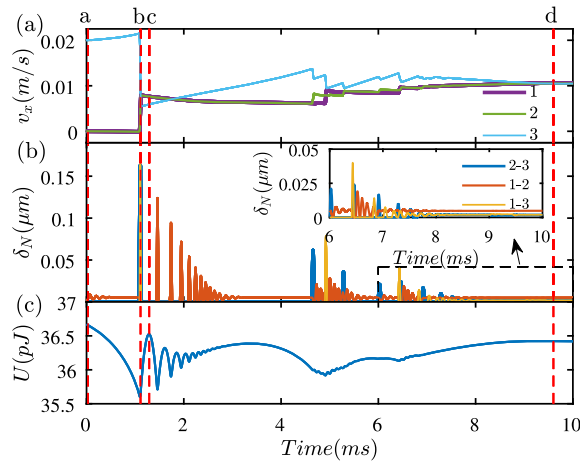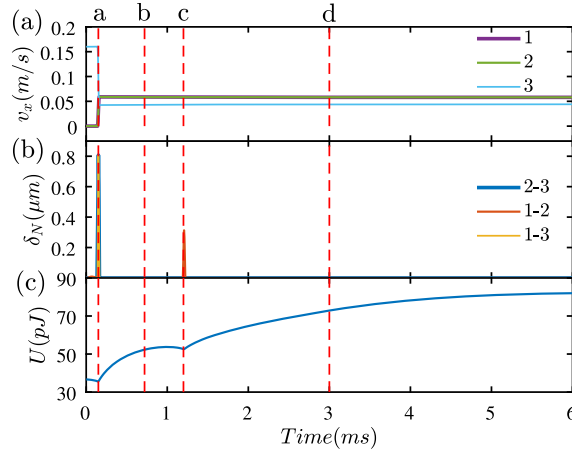
Fig. 13. Temporal evolution of (a) the velocity along the x direction, (b) the inter-particle overlaps and (c) the total electrostatic energy in the collision process shown in Fig. 12. Vertical dashed lines correspond to different instants in Fig. 12.
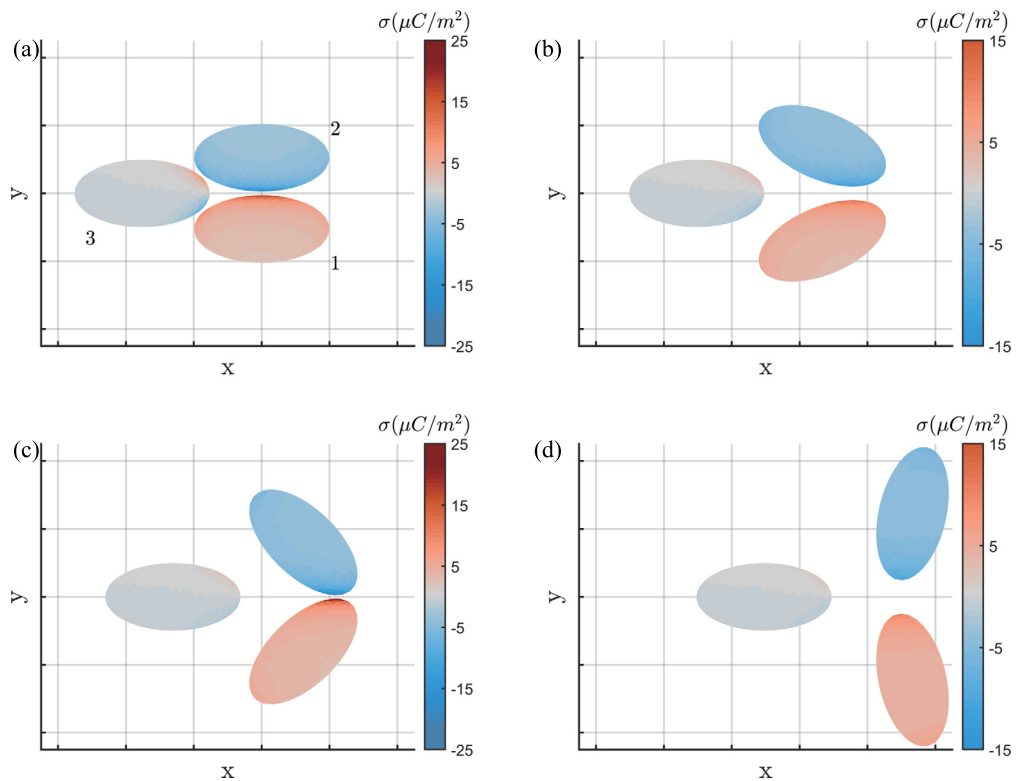
Fig. 14. Snapshots of the collision process between ellipsoid 3 and the side-by-side aggregate formed by ellipsoids 1 and 2 at (a) $t = 0.15$ ms, (b) $t = 0.72$ ms, (c) $t = 1.2$ ms and (d) $t = 3$ ms. The incident velocity of ellipsoid 3 is $v_0 = 0.16$ m/s along the x direction.

and 2 fall back and collide again, and this process repeats several times, which is marked by multiple orange peaks of δ_N (between particle 1 and 2) in Fig. 13(b). The peak height drops as the number of collision increases, because the restitution coefficient is smaller than unity and the kinetic energy is thus effectively damped after each collision. Eventually, when all the relative kinetic energy is dissipated, particle 3 is captured and three primary particles stick together, moving together as a new aggregate (Fig. 12(d)). The interparticle overlaps in this state are determined by the balance between the electrostatic attraction and the elastic repulsion (shown in the inset of Fig. 13(b)).

Fig. 14 shows several snapshots of a collision-induced fragmentation process. The initial configuration is the same as shown in Fig. 12(a) except for a large incident velocity $v_0 = 0.16$ m/s of particle 3. After the first collision, particle 1 and 2 contained in the original aggregate obtain a larger translation velocity (Fig. 15(a)) and separate with a high rotation rate.

Fig. 15. Temporal evolution of (a) the velocity along the x direction, (b) the inter-particle overlaps and (c) the total electrostatic energy in the collision process shown in Fig. 14. Vertical dashed lines correspond to different instants in Fig. 14.

As they separate and rotate, their tails collide at $t = 1.2$ ms (Fig. 15(b)) at a high velocity. The resulting rebound velocity is so large that particle 1 and 2 cannot be pulled back together through their electrostatic attraction. As they continue to move apart, the electrostatic energy increases, as shown in Fig. 15(c). As expected, if incident particle brings in sufficient kinetic energy to overcome the electrostatic cohesion between charged particles in an aggregate, instead of being captured and forming a new aggregate, the incident particle will fragment the entire aggregate. Unlike the spherical counterpart, this process is much more complicated for non-spherical cases as the particle orientation, aggregate configuration, and incident angle could all affect the final results. Nevertheless, the simulation framework is shown to successfully capture the electrostatic energy changes in this process.

4. Conclusion

In this study, a numerical framework is developed to simulate the interaction of charged dielectric particles with non-spherical shapes. For non-spherical geometries, local interactions are strongly affected by local surface charges and the local surface curvature. The framework accurately resolves local interactions by employing the boundary element method (BEM) to resolve local charge distributions between non-spherical particles. The method is accelerated using the GMRES-FMM coupled calculation, and the scaling between the computational time and the number of surface patches reduces significantly. The method is validated using several cases: (i) potential energy of a point charge interacting with a sphere (Appendix A), (ii) forces between two charged spheres with different separations, (iii) torque acted on dielectric particles with different shapes exerted by an external field, (iv) electrostatic force between two charged prolate spheroids with different separations and orientations.

While studying these validation cases, we find that BEM captures the multipole electrostatic interactions between charged dielectric particles, which may be more important than the Coulomb force when the particle separation is smaller than the particle diameter.

Furthermore, the particle shape amplifies the induced charge effect, which highlights the importance of conducting BEM calculation for non-spherical geometries. Two important consequences of non-spherical geometries have been identified: (i) the induced charge density is sensitive to the local curvature of the particle, and (ii) the electrostatic interactions are sensitive to the particle orientation. Neither of these features can be captured by the classical Coulomb or the dipole interactions.

Finally, to complete the framework, the contact forces/toques are included to resolve inter-particle collisions. A reduced stiffness is applied to increase the collision time step and to reduce the calculation cost, and the double-shell model is proposed to prevent the intersection between different surface patches. To avoid introducing extra errors in the calculation, the thickness of the buffer layer is chosen when the electrostatic energy between two particles saturates.

In addition, by performing dynamic simulations of particle-aggregate collisions, different collision outcomes are reproduced, including sticking and fragmentation. The evolution of the collision process and the electrostatic interaction are also displayed to help understand the underlying physics.

In the present framework, the simulation is assumed to be in vacuum, so particles are only affected by electrostatic and contact interactions. When the surrounding medium becomes gas or liquid, it brings two effects: (a) different medium permittivity and dielectric constant, and (b) particle-fluid interactions. The first effect can be accounted for by adjusting κ_0 and ε_0. The second effect involves a fluid solver dedicated to the couplings between the two phases. Since this solver is independent from the electrostatic calculation in this paper, it will not affect the numerical stability [36,9,47]. Furthermore, the computational cost of the particle-fluid interactions is associated with the number of particles, N_p, while the cost of
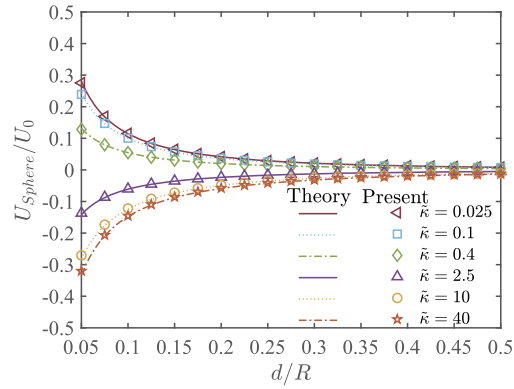
Fig. 16. Normalized potential energy between a point charge and a dielectric sphere.

the introduced electrostatic calculation is related to the total number of surface patches, N. Considering that $N = nN_p$ and $n = O(10^2 - 10^3)$, the electrostatic computation will be the most computationally intensive part, so adding the fluid-particle interaction should be feasible without adding too much extra computational cost.

Based on the present study, several interesting directions may be worth pursuing. First, the present study deals with the ellipsoidal particles using the quadratic expression. By adopting other general expressions, this framework can be extended to more non-spherical shapes, e.g. arbitrary convex particles [20,8]. Second, the simulation conditions in Section 3.3 are comparable to the previous study by Lee et al. [28], where the binding energy from electrostatic interactions is three orders of magnitude larger than that from short-range cohesion. Thus, the van der Waals interaction is of minor impact. However, for smaller particles or lower charging density, the van der Waals interaction can be more important. In such cases, since the Hertzian contact model is already implemented, the current framework can be easily extended to include the van der Waals interaction [36,29]. Investigating how the presence of electrostatic interactions affects the adhesion processes at the microparticle scale may provide key insights into the physics behind these processes [24]. Furthermore, the triboelectrification between dielectric particles is a long-lasting yet unsettled problem. By incorporating certain models of charge transfer in collisions, the present framework can be applied to test different charge transfer models and help unveil the mysterious mechanism behind tribocharging [38,27,25].

CRediT authorship contribution statement

Xuan Ruan: Data curation, Formal analysis, Investigation, Methodology, Writing – original draft. **Matthew T. Gorman:** Investigation, Methodology, Writing – review & editing. **Shuiqing Li:** Funding acquisition, Supervision, Writing – review & editing. **Rui Ni:** Conceptualization, Funding acquisition, Project administration, Supervision, Writing – review & editing.

Declaration of competing interest

The authors declare that they have no known competing financial interests or personal relationships that could have appeared to influence the work reported in this paper.

Acknowledgement

Appendix A. Validation of the electrostatic calculation

The electrical potential energy U between a point charge q and a neutral dielectric sphere is given by Jackson [21], Barros and Luijten [3] as

$$U = \frac{q^2}{8\pi\varepsilon_0\kappa_m R} \sum_{n=0}^{\infty} \frac{(1-\tilde{\kappa})n}{(1+\tilde{\kappa})n+1} \frac{1}{1+(1+d/R)^{2(n+1)}}, \tag{53}$$

where κ_m and κ_p are the dielectric constants of the medium and the sphere, $\tilde{\kappa} = \kappa_p/\kappa_m$ is their ratio. d is the distance from the point charge to the surface of the sphere, R is the sphere radius. The electrical energy U is normalized by $U_0 = q^2/\varepsilon_0\kappa_m R$ and shown in Fig. 16. The BEM results show good agreement with the theoretical solutions, which validates our

calculation. When the point charge is close to the sphere, deviations may occur due to the limited surface patch number. Increasing the total patch number or refining the local surface patches could further improve the accuracy. Here, the total surface patch number $N_{patch} = 956$ is used to achieve high accuracy for $d/R = 0.05$.

References

[1] S. Alfano, M.L. Greer, Determining if two solid ellipsoids intersect, J. Guid. Control Dyn. 26 (2003) 106–110, https://doi.org/10.2514/2.5020.
[2] E. Allahyarov, E. Zaccarelli, F. Sciortino, P. Tartaglia, H. Löwen, Interaction between charged colloids in a low dielectric constant solvent, Europhys. Lett. 78 (2007) 38002.
[3] K. Barros, E. Luijten, Dielectric effects in the self-assembly of binary colloidal aggregates, Phys. Rev. Lett. 113 (2014) 017801, https://doi.org/10.1103/PhysRevLett.113.017801, https://link.aps.org/doi/10.1103/PhysRevLett.113.017801.
[4] K. Barros, D. Sinkovits, E. Luijten, Efficient and accurate simulation of dynamic dielectric objects, J. Chem. Phys. 140 (2014) 064903, https://doi.org/10.1063/1.4863451.
[5] H.T. Baytekin, A.Z. Patashinski, M. Branicki, B. Baytekin, S. Soh, B.A. Grzybowski, The mosaic of surface charge in contact electrification, Science 333 (2011) 308–312, https://doi.org/10.1126/science.1201512, https://www.science.org/doi/abs/10.1126/science.1201512.
[6] M.A. Behjani, N. Rahmanian, N. Fardina bt Abdul Ghani, A. Hassanpour, An investigation on process of seeded granulation in a continuous drum granulator using dem, Adv. Powder Technol. 28 (2017) 2456–2464, https://doi.org/10.1016/j.apt.2017.02.011.
[7] E. Bichoutskaia, A.L. Boatwright, A. Khachatourian, A.J. Stace, Electrostatic analysis of the interactions between charged particles of dielectric materials, J. Chem. Phys. 133 (2010) 024105.
[8] C. Boon, G. Houlsby, S. Utili, A new contact detection algorithm for three-dimensional non-spherical particles, Powder Technol. 248 (2013) 94–102.
[9] E. Capecelatro, O. Desjardins, An Euler-Lagrange strategy for simulating particle-laden flows, J. Comput. Phys. 238 (2013) 1–31, https://doi.org/10.1016/j.jcp.2012.12.015.
[10] S. Chen, W. Liu, S. Li, Effect of long-range electrostatic repulsion on pore clogging during microfiltration, Phys. Rev. E 94 (2016) 063108.
[11] S. Chen, W. Liu, S. Li, A fast adhesive discrete element method for random packings of fine particles, Chem. Eng. Sci. 193 (2019) 336–345, https://doi.org/10.1016/j.ces.2018.09.026, https://www.sciencedirect.com/science/article/pii/S0009250918306754.
[12] J. Chesnutt, J. Marshall, Blood cell transport and aggregation using discrete ellipsoidal particles, Comput. Fluids 38 (2009) 1782–1794.
[13] M. Di Renzo, J. Urzay, Aerodynamic generation of electric fields in turbulence laden with charged inertial particles, Nat. Commun. 9 (2018) 1–11.
[14] J.Q. Feng, Electrostatic interaction between two charged dielectric spheres in contact, Phys. Rev. E 62 (2000) 2891.
[15] Z. Gimbutas, L. Greengard, Computational software: simple fmm libraries for electrostatics, slow viscous flow, and frequency-domain wave propagation, Commun. Comput. Phys. 18 (2015) 516–528, https://doi.org/10.4208/cicp.150215.260615sw.
[16] L. Greengard, V. Rokhlin, A fast algorithm for particle simulations, J. Comput. Phys. 73 (1987) 325–348.
[17] C. Güttler, J. Blum, A. Zsom, C.W. Ormel, C.P. Dullemond, The outcome of protoplanetary dust growth: pebbles, boulders, or planetesimals?-I. Mapping the zoo of laboratory collision experiments, Astron. Astrophys. 513 (2010) A56.
[18] J. Hærvig, U. Kleinhans, C. Wieland, H. Spliethoff, A.L. Jensen, K. Sørensen, T.J. Condra, On the adhesive jkr contact and rolling models for reduced particle stiffness discrete element simulations, Powder Technol. 319 (2017) 472–482.
[19] J.M. Harper, G. McDonald, J. Dufek, M. Malaska, D. Burr, A. Hayes, J. McAdams, J. Wray, Electrification of sand on titan and its influence on sediment transport, Nat. Geosci. 10 (2017) 260–265.
[20] G. Houlsby, Potential particles: a method for modelling non-circular particles in dem, Comput. Geotech. 36 (2009) 953–959.
[21] J. Jackson, Classical Electrodynamics, Wiley, 1999.
[22] A. Jaworek, A. Marchewicz, A. Sobczyk, A. Krupa, T. Czech, Two-stage electrostatic precipitators for the reduction of pm2. 5 particle emission, Prog. Energy Combust. Sci. 67 (2018) 206–233.
[23] J. Jones, Electromechanics of Particles, Cambridge University Press, 1995.
[24] F. Jungmann, T. Steinpilz, J. Teiser, G. Wurm, Sticking and restitution in collisions of charged sub-mm dielectric grains, J. Phys. Commun. 2 (2018) 095009.
[25] A.G. Kline, M.X. Lim, H.M. Jaeger, Precision measurement of tribocharging in acoustically levitated sub-millimeter grains, Rev. Sci. Instrum. 91 (2020) 023908.
[26] J. Kolehmainen, A. Ozel, Y. Gu, T. Shinbrot, S. Sundaresan, Effects of polarization on particle-laden flows, Phys. Rev. Lett. 121 (2018) 124503.
[27] D.J. Lacks, T. Shinbrot, Long-standing and unresolved issues in triboelectric charging, Nat. Rev. Chem. 3 (2019) 465–476.
[28] V. Lee, S.R. Waitukaitis, M.Z. Miskin, H.M. Jaeger, Direct observation of particle interactions and clustering in charged granular streams, Nat. Phys. 11 (2015) 733–737.
[29] S. Li, J.S. Marshall, G. Liu, Q. Yao, Adhesive particulate flow: the discrete-element method and its application in energy and environmental engineering, Prog. Energy Combust. Sci. 37 (2011) 633–668.
[30] S.Q. Li, J. Marshall, Discrete element simulation of micro-particle deposition on a cylindrical fiber in an array, J. Aerosol Sci. 38 (2007) 1031–1046, https://doi.org/10.1016/j.jaerosci.2007.08.004.
[31] I.V. Lindell, J.C.E. Sten, K.I. Nikoskinen, Electrostatic image method for the interaction of two dielectric spheres, Radio Sci. 28 (1993) 319–329.
[32] E.B. Lindgren, A.J. Stace, E. Polack, Y. Maday, B. Stamm, E. Besley, An integral equation approach to calculate electrostatic interactions in many-body dielectric systems, J. Comput. Phys. 371 (2018) 712–731, https://doi.org/10.1016/j.jcp.2018.06.015.
[33] E.B. Lindgren, B. Stamm, Y. Maday, E. Besley, A.J. Stace, Dynamic simulations of many-body electrostatic self-assembly, Philos. Trans. Royal Soc. A, Math. Phys. Eng. Sci. 376 (2018) 20170143.
[34] G. Liu, J. Marshall, S. Li, Q. Yao, Discrete-element method for particle capture by a body in an electrostatic field, Int. J. Numer. Methods Eng. 84 (2010) 1589–1612.
[35] J. Lu, R.A. Shaw, Charged particle dynamics in turbulence: theory and direct numerical simulations, Phys. Fluids 27 (2015) 065111.
[36] J. Marshall, Discrete-element modeling of particulate aerosol flows, J. Comput. Phys. 228 (2009) 1541–1561, https://doi.org/10.1016/j.jcp.2008.10.035.
[37] A. Matias, T. Shinbrot, N. Araújo, Mechanical equilibrium of aggregates of dielectric spheres, Phys. Rev. E 98 (2018) 062903.
[38] L.S. McCarty, G.M. Whitesides, Electrostatic charging due to separation of ions at interfaces: contact electrification of ionic electrets, Angew. Chem., Int. Ed. Engl. 47 (2008) 2188–2207.
[39] Y. Nakajima, T. Sato, Calculation of electrostatic force between two charged dielectric spheres by the re-expansion method, J. Electrost. 45 (1999) 213–226, https://doi.org/10.1016/S0304-3886(98)00051-5.
[40] H. Ohshima, Electrostatic interaction between two dissimilar spheres with constant surface charge density, J. Colloid Interface Sci. 170 (1995) 432–439.
[41] H. Ohshima, E. Mishonova, E. Alexov, Electrostatic interaction between two charged spherical molecules, Biophys. Chem. 57 (1996) 189–203.
[42] P.O. Persson, G. Strang, A simple mesh generator in matlab, SIAM Rev. 46 (2004) 329–345.
[43] X. Qian, X. Ruan, S. Li, Effect of interparticle dipolar interaction on pore clogging during microfiltration, Phys. Rev. E 105 (2022) 015102, https://doi.org/10.1103/PhysRevE.105.015102, https://link.aps.org/doi/10.1103/PhysRevE.105.015102.

[44] J. Qin, J.J. de Pablo, K.F. Freed, Image method for induced surface charge from many-body system of dielectric spheres, J. Chem. Phys. 145 (2016) 124903.

[45] X. Ruan, S. Chen, S. Li, Structural evolution and breakage of dense agglomerates in shear flow and Taylor-Green vortex, Chem. Eng. Sci. 211 (2020) 115261, https://doi.org/10.1016/j.ces.2019.115261.

[46] X. Ruan, S. Chen, S. Li, Effect of long-range Coulomb repulsion on adhesive particle agglomeration in homogeneous isotropic turbulence, J. Fluid Mech. 915 (2021).

[47] Y. Shao, X. Ruan, S. Li, Mechanism for clogging of microchannels by small particles with liquid cohesion, AIChE J. 67 (2021) e17288, https://doi.org/10.1002/aic.17288, https://aiche.onlinelibrary.wiley.com/doi/abs/10.1002/aic.17288.

[48] D. Song, P. Mehrani, Mechanism of particle build-up on gas-solid fluidization column wall due to electrostatic charge generation, Powder Technol. 316 (2017) 166–170.

[49] T. Steinpilz, K. Joeris, F. Jungmann, D. Wolf, L. Brendel, J. Teiser, T. Shinbrot, G. Wurm, Electrical charging overcomes the bouncing barrier in planet formation, Nat. Phys. 16 (2020) 225–229.

[50] J. Telling, J. Dufek, A. Shaikh, Ash aggregation in explosive volcanic eruptions, Geophys. Res. Lett. 40 (2013) 2355–2360.

[51] C. Thornton, K. Yin, Impact of elastic spheres with and without adhesion, Powder Technol. 65 (1991) 153–166, https://doi.org/10.1016/0032-5910(91)80178-L, https://www.sciencedirect.com/science/article/pii/003259109180178L, a Special Volume Devoted to the Second Symposium on Advances in Particulate Technology.

[52] K. Washino, E.L. Chan, T. Tanaka, Dem with attraction forces using reduced particle stiffness, Powder Technol. 325 (2018) 202–208.

[53] M. Washizu, Precise calculation of dielectrophoretic force in arbitrary field, J. Electrost. 29 (1993) 177–188.